Open Access

Recent Progress in Materials

LIDSEN Publishing Inc.

Original Research

Stress Analysis and Life Prediction of a Ceramic Matrix Composite Vane Using a Micromechanics-Based Approach

Unni Santhosh *, Jalees Ahmad

Structural Analytics, Inc., Carlsbad, CA 92010, US; E-Mails: usanthosh@structuralanalyticsinc.com; jahmad@structuralanalyticsinc.com

* **Correspondence:** Unni Santhosh; E-Mail: usanthosh@structuralanalyticsinc.com

Academic Editor: Ali Abdul-Aziz

Special Issue: Ceramic Matrix Composites: Performance Evaluation and Application

Recent Progress in Materials
2023, volume 5, issue 4
doi:10.21926/rpm.2304035

Received: September 06, 2023
Accepted: November 27, 2023
Published: December 01, 2023

Abstract

The results of stress analysis of a ceramic matrix composite (CMC) vane using a physics-based model developed for two-dimensional woven CMCs are presented. The model considers the inherent defects and micromechanical damage in woven CMCs along with time-dependent deformation of the constituents. Predictions include damage state under general load conditions and the global deformation response of the vane. Strain-gage data from burst tests are compared to strain predictions obtained using the model. Results from time-dependent analysis and life prediction of the vane under constant loads and cyclic loads at elevated temperatures are presented. Effect of fatigue frequency on the deformation and long-term life of the vane are also discussed.

Keywords

Ceramic matrix composite; vane; modeling; stress analysis; life prediction

1. Introduction

The high efficiency and regulatory requirements demanded of the next generation aircraft engines impose severe constraints on the selection of structural materials that can be used in building them. The high temperature capability combined with their low density as compared to titanium and nickel-based alloys make ceramics and their composite derivatives ideal candidate materials for the hot sections of turbine engines tailored for these requirements [1]. The use of these materials allows for the potential operation of gas turbines at higher inlet temperatures without the need for external cooling, which in turn reduces the overall weight while increasing efficiency and reducing the noise level during engine operation while maintaining low Nitrogen Oxide (NOx) and Carbon Monoxide (CO) emissions [2, 3]. Furthermore, as compared to monolithic ceramics the reinforcements in ceramic matrix composites (CMCs) give them superior toughness and durability even at elevated temperatures [4].

Uses of CMCs however add complexities in part fabrication [5]. Considerable advances have been made since the 1980s in using CMCs to make combustor liners [6-8], nozzle flaps [7, 9], vanes [8, 10-13], blades [14], bladed disks [15], and shrouds [16, 17], though a number of these applications remain experimental. Commercially, the major aircraft engine companies have made significant investments in the development and manufacture of CMC hot-section components for use in turbine engines [18, 19] and, in some cases, CMC parts are currently being flown on civilian aircrafts [20].

Currently, a safe life approach [21] that requires the use of test data obtained from extensive material testing done under flight-critical load conditions is the preferred method used to design aerospace turbine engine hot section CMC components [22]. While material testing is important to understand the deformation and failure mechanisms that may sometimes be unique to these materials and to generate a design database, this approach to part design is ultimately time-consuming and cost-prohibitive, leading to long development times and expensive parts. Therefore, there is a need for a robust deformation modeling and life prediction approach that incorporates these deformation mechanisms in order to apply the material technology to product design in a cost-effective manner [22]. Lacking such a modeling approach testing will have to be done each time the composite configuration and/or loading is changed significantly. A sufficiently well validated model will be able to predict the effect of stress raisers, such as holes and notches, without further extensive testing. A mechanics-based model will also be able to determine the residual life of the composite part during service, which will be of significant benefit from inspection, replacement, and life-cycle cost considerations.

Remarkable progress has been achieved over the past several years in understanding and modeling of various deformation and damage mechanisms in CMCs, especially in two-dimensional (2D) woven silicon carbide/silicon carbide (SiC/SiC) composites up to 1200°C. Models have been developed for dominant deformation and damage mechanisms in these composites under various load and temperature conditions relevant to engine operating conditions, including the effect of environmental degradation. References [23-39] describe some such material models for CMCs. The general approaches used to model the structural response of CMCs consists of either considering the CMC as a homogeneous orthotropic material in combination with continuum damage mechanics [23, 24, 31-34], or using micromechanics to combine models representing the damage and deformation mechanisms in each of the individual constituents of the composite [25, 26, 28, 30,

35, 36, 39]. Typically, when micromechanics is used, large structures are modeled either using a unit-cell approach that captures the constitutive behavior of the CMC [25, 26, 28], or using a multiscale approach that models the CMC at different length scales [30, 35, 36, 39]. The underlying physics is predicted in greater detail depending on the modeling approach used. However, this comes at greater computational cost. In general, solution fidelity and solution times, both, are the least when the CMC is modeled as a homogeneous and single material and is the greatest in the case of multiscale approaches. To be practical and cost-effective, analysis of large CMC structures thus requires the right balance of solution fidelity and computational efficiency [40].

Some of the models in the references listed above have been implemented into finite element (FE) structural analysis codes (for example, see [40, 41]). These physics-based models use material properties and model constants determined by characterizing data from simple tension and creep test specimens under unidirectional loading. In most cases, limited validation of their predictive accuracy has been done by direct comparison with measured response of coupon-level test specimens under laboratory conditions. Further validation of the models by successfully modeling more representative CMC structures is needed before their eventual use in aiding turbine engine hot-section component design. However, one challenge to achieve this is the limited availability of relevant published experimental data from well-instrumented tests to sufficiently assess the models due to the often proprietary and security-related nature of most CMC applications.

A search of the published literature by the authors identified experimental data from a study [10, 42] on the fabrication and instrumented burst testing of a CMC vane subelement to be suitable for structural modeling. In the present paper, the CMC vane described in [42] is modeled and studied using the FE method combined with a physics-based CMC material model that combines matrix microcracking, constituent creep and SiC oxidation. A brief description of the CMC model is initially presented. Composite properties obtained from flat test coupons are used as inputs to the model in order to characterize deformation and failure of the vane subjected to increasing internal pressure loading. Finally, the time to failure (service life) of the vane is predicted when the pressure load is held constant and when the load is cycled.

2. Deformation Model for CMCs

The CMC model used in the stress analysis of the vane is based on a unit-cell approach. In this model the 2D woven composite is considered as having fiber and matrix; one constituent is assumed to be brittle while the other can exhibit viscoplastic behavior. Experimental observations [43] show that matrix in CMCs undergoes progressive microcracking under load. The density of microcracks increases with load and the final failure of the material is preceded by the fracture of fibers. The present model considers the composite as an assemblage of damaged and undamaged unit-cells (Figure 1(a)). Damage within the cells consists of matrix cracks transverse to the load direction, and longitudinal cracks in the matrix or fiber-matrix disbonds. Here the load direction is considered to be aligned along the fiber direction in a unidirectional composite and along one of the fiber directions in a cross-ply system. The cracks are described by parameters η and ρ that are given by the ratio of the length of the crack to the length of the composite in the direction of the crack. Thus, η represents the proportion of the unit-cell width that is cracked while ρ represents the proportion of the length of the unit-cell over which there is no shear load transfer between the fiber and the

matrix. Further, the model assumes that under increasing load these parameters follow a Weibull type curve that simulates the increasing crack density in the composite.

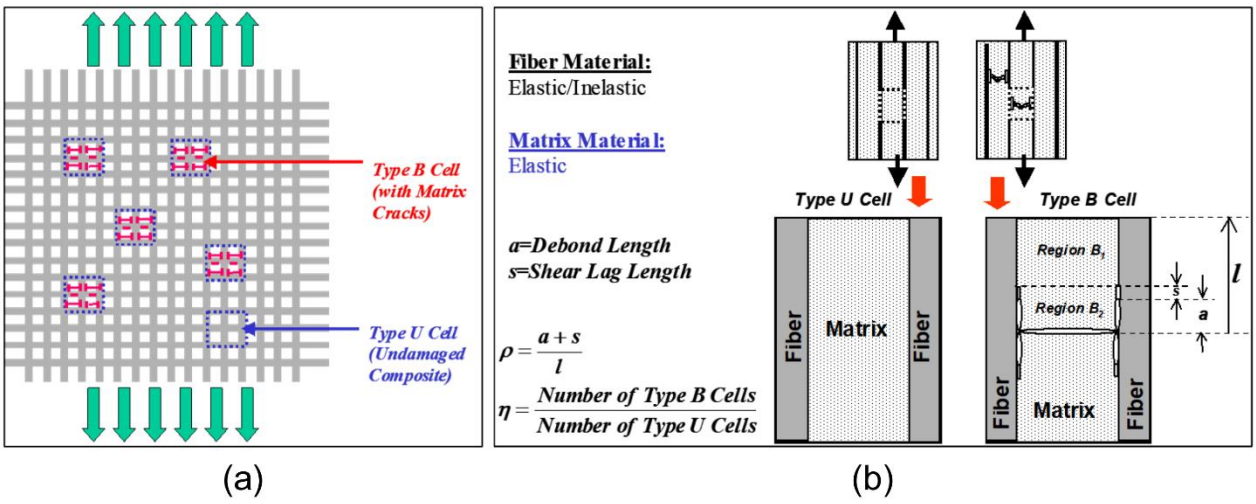

Figure 1 (a) CMC Damage Model and **(b)** Unit Cells in CMC Damage Model.

The transverse and longitudinal cracks associated by the parameters η and ρ, respectively, divide the unit-cell into three regions, U, B_1 and B_2, as shown in Figure 1(b). Initially, assuming no initial damage, the composite contains only U-type cells. With the assumptions stated above, η and ρ increases progressively along with the volume fraction of the associated B and B_2 cells. Assuming iso-strain condition in the direction of the load, we can use the rule-of-mixtures and the inverse-rule-of-mixtures formulations to derive the strain rate in the composite. This derivation has been described in detail in [28] and the final expression for the strain rate in the load direction can be written as:

$$\begin{aligned}\dot{\varepsilon} = {} & \frac{1}{[1+F(1-\eta)E_U]} \\ & \left\{F\left[\dot{\sigma}+\frac{\dot{\eta}}{\eta}(\sigma_U-\sigma)-(1-\eta)\frac{\dot{E}_U}{E_U}\sigma_U\right]+\right. \\ & \left[H\eta\dot{\rho}-\frac{(1-\rho)}{E_U^2}\dot{E}_U-\frac{\rho}{E_{B_2}^2}\dot{E}_{B_2}\right]\frac{[\sigma-(1-\eta)\sigma_U]}{\eta} \\ & +F(1-\eta)E_U\dot{\varepsilon}_U^I+(1-\rho)\dot{\varepsilon}_{B_1}^I+\rho\dot{\varepsilon}_{B_2}^I+\left(\varepsilon_{B_2}^I-\varepsilon_{B_1}^I\right)\dot{\rho} \\ & +F(1-\eta)E_U\left(\dot{\alpha}_U\Delta T+\alpha_U\dot{T}\right)+(1-\rho)\dot{\alpha}_U\Delta T+\rho\dot{\alpha}_{B_2}\Delta T \\ & \left.+\left(\alpha_U\Delta T+\rho\alpha_{B_2}\right)\dot{T}+\left(\alpha_{B_2}-\alpha_U\right)\Delta T\dot{\rho}\right\}, \text{for } \eta\neq 0 \text{ or } \rho\neq 0 \end{aligned} \quad (1a)$$

$$\dot{\varepsilon}=\frac{\dot{\sigma}}{E_U}-\frac{\dot{E}_U}{E_U^2}\sigma+\dot{\alpha}_U\Delta T+\alpha_U\dot{T}+\frac{E'_m\nu'_m}{E_U}\dot{\varepsilon}_{m_U}^{I'}+\frac{\nu'_m}{E_U}\left(\dot{E}_m-\frac{E'_m}{E_U}\dot{E}_U\right)\varepsilon_{m_U}^{\prime I}, \text{for } \eta=\rho=0 \quad (1b)$$

where $F=\frac{1}{\eta}\left(\frac{1-\rho}{E_U}+\frac{\rho}{E_{B_2}}\right)$, $H=\frac{1}{\eta}\left(\frac{1}{E_{B_2}}-\frac{1}{E_U}\right)$ and

$$\dot{\varepsilon}_{B_1}=\frac{B}{E_U}-\frac{A}{E_U^2}\dot{E}_U+\dot{\alpha}_U\Delta T+\alpha_U\dot{T}+\dot{\varepsilon}_{B_1}^I \quad (1c)$$

$$\dot{\varepsilon}_{B_2} = \frac{B}{E_{B_2}} - \frac{A}{E_{B_2}^2}\dot{E}_{B_2} + \dot{\alpha}_{B_2}\Delta T + \alpha_{B_2}\dot{T} + \dot{\varepsilon}_{B_2}^{I} \tag{1d}$$

In the above expressions,

$$A = \frac{\sigma - (1-\eta)\sigma_U}{\eta} \text{ and}$$

$$B = \frac{1}{\eta}\left[\dot{\sigma} - (1-\eta)\left\{E_U\left(\dot{\varepsilon} - \dot{\varepsilon}_U^I - \dot{\alpha}_U\Delta T - \alpha_U\dot{T}\right) + \frac{\dot{E}_u}{E_u}\sigma_U\right\} - (\sigma - \sigma_U)\frac{\dot{\eta}}{\eta}\right] \tag{1e}$$

Here *E*'s and *α*'s are the Young's modulus and the coefficients of thermal expansion, *v* the volume fraction, subscripts *f* and *m* denote fiber and the effective-matrix[1], *U*, B_1 and B_2 the regions in Figure 1, *σ* is the stress, *T* the temperature and '.' denotes the time rate of the variable in the equation. Then the strain rate just due to damage is simply

$$\dot{\varepsilon}^D = \dot{\varepsilon}(\eta, \rho) - \dot{\varepsilon}(0,0) \tag{2}$$

In this model the functions *η* and *ρ* describing the evolution of the damage are expressed in terms of the Weibull statistics function as

$$\eta(t) = 1 - exp\left[-0.693\left(\frac{\sigma_m}{\sigma_0}\right)^{\eta_n}\right] \tag{3a}$$

and

$$\rho(t) = 1 - exp\left[-\rho_{nc}\left(\frac{\sigma_m}{\sigma_0}\right)^{\rho_{nn}}\right] \tag{3b}$$

Here σ_0 is a matrix strength parameter defined such that $\eta(t) = 0.5$ when $\sigma_m = \sigma_0$. The parameters, σ_0, η_n, ρ_{nc} and ρ_{nn} in equations (3) are obtained by calibrating the tensile stress-strain response of the CMC at specific temperatures.

Similarly, fiber fracture is described in the model in terms of the following Weibull statistics-based expression:
and

$$\psi(t) = 1 - \exp\left[-0.693\left(\frac{\sigma_f - \sigma_{fm}}{\sigma_{f0} - \sigma_{fm}}\right)^{\psi_n}\right] \tag{3c}$$

where σ_{f0} is the fiber strength parameter that corresponds to half the fibers failing ($\psi(t) = 0.5$) when $\sigma_f = \sigma_{f0}$, σ_{fm} is the minimum stress when fibers start to fracture, and the parameter ψ_n defines the progressive fracture of fibers under increasing fiber stress, σ_f.

All the parameters describing damage in equations (3a), (3b) and (3c) are obtained at each temperature by exercising the model to 'fit' the measured tensile stress-strain response of the CMC at that temperature.

[1] Here the fiber refers to the coated fiber and the effective matrix is defined as a homogeneous equivalent material that includes the actual matrix constituent of the composite and the transverse coated fibers.

Time-dependent strain rate, $\dot{\varepsilon}_m^I$, of the constituent, which in these CMCs is the *in-situ* matrix (*m*), is modeled by the following modified form of the Bailey-Norton law:

$$\dot{\varepsilon}_m^I = A{\sigma_m}^m(\varepsilon_m^I)^n \tag{4a}$$

Here σ_m is the stress in the matrix and *A*, *n* and *m* are material constants. In addition, the matrix strain rate is limited to a minimum value, β, i.e.,

$$\dot{\varepsilon}_m^I \leq \beta \tag{4b}$$

This limiting condition is based on observation of creep and two-hour dwell fatigue data from the Sylramic™-iBN/ melt-infiltrated SiC (0101 CMC) CMC that shows that the secondary slope reaches a limiting non-zero value at large times [44].

This approach has been used in Reference [28] to model the tensile response of several CMCs with a wide range of non-linear stress-strain behavior and in Reference [44] to model the creep and dwell-fatigue behaviors of the 0101 CMC. The solution procedure uses a numerical technique such as the Runge-Kutta method to solve the non-linear equations. It has also been shown in [28] that the product $\eta^*\rho$ which can be interpreted as a measure of the crack-density in the composite shows the same qualitative behavior as the crack-density estimated in experiments using acoustic energy data.

The model has also been extended to the case where in-plane shear is present [45] in a 2D woven CMC. The nature of the weave and the loading of the vane sub-element considered in the present study is such that in-plane shear does not play a significant role in determining deformation and failure. Thus, in-plane shear was not considered in this study and a description of the shear model is not presented.

SiC/SiC CMCs are known to degrade when exposed to oxidizing environment at elevated temperatures [46]. The cracked matrix allow environment to enter and oxidize the fiber and reducing the area over which it can carry load. The stress on the SiC fiber thus increases continuously until rupture.

Oxidation kinetics of the SiC constituents and its effect on the composite response has been incorporated into the forementioned model as described in Reference [47]. The conceptional view of the combined damage-deformation-oxidation model is shown in Figure 2. Under a given set of transient mechanical load and transient temperature conditions, the progressive damage model determines deformations and stresses in the constituent materials (fiber, matrix, and fiber coatings) within the composite as well as the distribution of damage in the form of microcracks in the matrix, interfacial separations, and fiber fracture. The microcracks provide pathways for the oxidizing environment to access the interior of the composite and the damage function η provides a measure of the fraction of fibers that are exposed to the environment. Thus, increase in external load results in more microcracking and thus η, and a corresponding increase in the fraction of fibers exposed to the environment. The chemical kinetics models associated with oxidation of each of the constituents determine the oxide thickness growth and the surface recession (material loss) of the constituents, both of which translates to decreases in their respective volume fractions. Uncoated SiC fibers start to oxidize as soon as they become exposed to the environment while oxidation of coated fibers will start to occur after volatilization of the coating becomes complete. Volume fractions of the oxidized constituents are updated in the damage and deformation model which subsequently evaluates the

redistribution of micromechanical stresses and associated increase in microcracking and creep. This time-dependent non-linear process is continued in the analysis, until a critical amount of fibers is determined to fail resulting in the final failure of the composite.

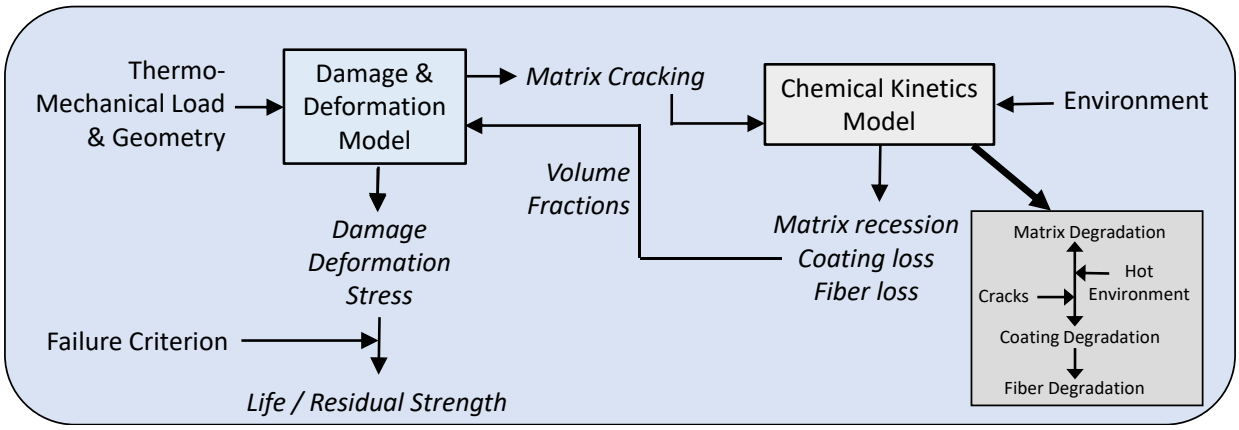

Figure 2 Combined oxidation-damage-deformation model.

For analysis of CMC structures, the above modeling procedure has been embedded in an in-house FE analysis code with implicit integration scheme such that each integration point within each element in the FE model follows the prescribed deformation and damage rules [48]. The FE procedure allows modeling of structural response and the consideration of macro-damage modes such as delaminations. The FE method combined with the above-described CMC constitutive model that includes shear [45] thus allows for analysis of three-dimensional CMC layup structures constructed using two-dimensional weaves. The damage and micromechanics-based approach has undergone significant theoretical and experimental validation by comparison of predictions and experimental measurements on a Sylramic™/melt-infiltrated SiC CMC [28, 44, 47, 48].

3. Material Description and Experimental Setup

The CMC material of the vane was developed under the Ultra Efficient Engine Technology (UEET) program [10, 42]. It consisted of Sylramic™ SiC fiber coated with in-situ Boron Nitride (iBN). Fabric of the fiber was woven by Albany Techni-Weave into a Y-cloth geometry in order to handle the anticipated high interlaminar stresses at the trailing edge of the vane. Figure 3 shows the fiber architecture and the Y-Cloth woven SiC/SiC composite used in vane fabrication. The vane sub-element consisted of six plies of Sylramic™ SiC fiber cloth with Chemical Vapor Infiltration (CVI), slurry cast and Melt Infiltrated matrix. The fabrication process is outlined in Reference [10].

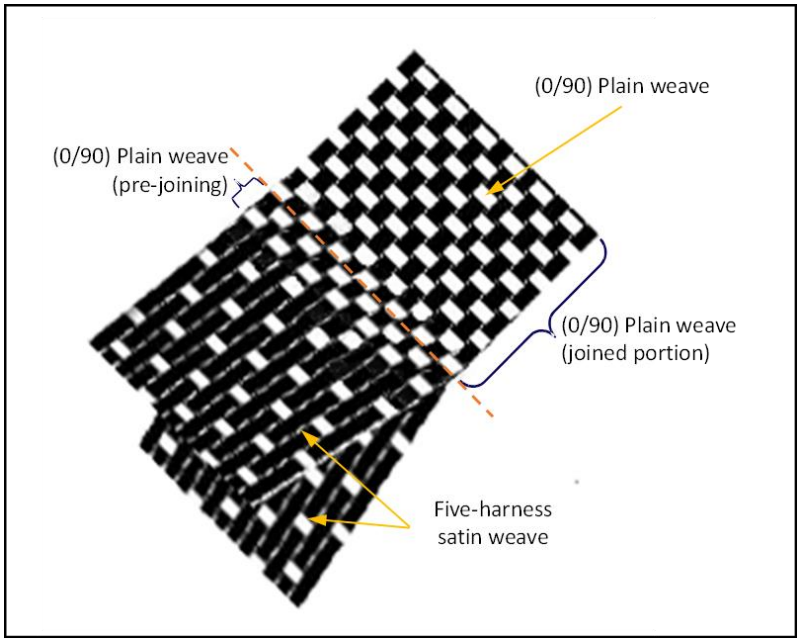

Figure 3 Modified Y-cloth geometry.

Since the primary application of the vane sub-elements was a demonstration in the High-Pressure Burner Rig (HPBR) at NASA Glenn Research Center the specimens were tested in the HPBR before being subjected to burst test. A total of six vane sub-elements were produced and two test specimens were cut from each vane. Figure 4 shows the typical vane geometry tested. The specimens were instrumented with strain-gages on its pressure and suction side in order to record the tension and compressive strains. The locations of the strain-gages are shown in Figure 5. Two specimens were mounted with five strain-gages each while each of the other ten vane specimens had two strain-gages. The vane specimens were subjected to monotonically increasing internal pressure at ambient temperature until failure. The loading was done using a flexible bladder, formed to the shape of the specimen cavity. Further details of the instrumentation and the testing are described in Reference [42].

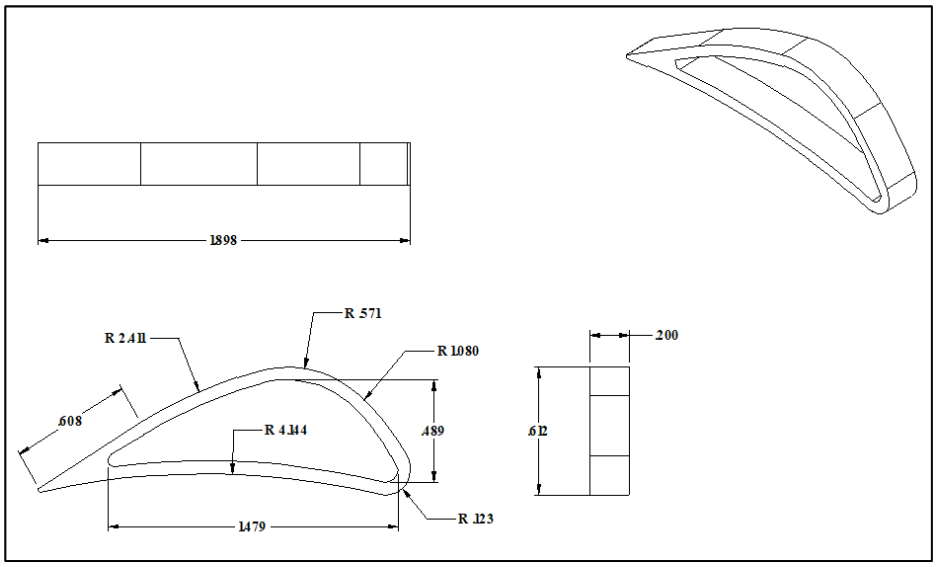

Figure 4 Geometry of the CMC vane test specimen.

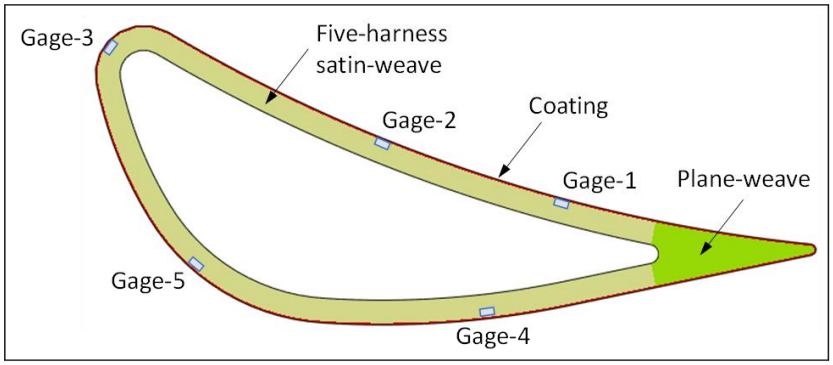

Figure 5 Material regions and strain-gage locations in CMC vane.

4. Estimation of Material Properties

The objective of the NASA research on the vane was to demonstrate the progress made in the design and fabrication techniques, developed under UEET, toward the application of CMC in cooled aerodynamic parts. In this regard the emphasis in the NASA project was to successfully make CMC blanks and to machine and test vane specimens. Comparison of the burst pressure and the failure mode was then made for vanes from different manufacturers. Since comparison of the strain response of the vanes was not the goal, the tensile stress-strain response of this material was not obtained. This material, with SiC fibers and SiC matrix with a fiber volume fraction of 40%, was expected to be nominally similar to the 0101 CMC material characterized in Reference [28]. Thus, in order to make the modeling of the vane more realistic it was decided to use the constituent properties from the 0101 CMC material along with the Y-cloth architecture of the vane CMC material and obtain a better estimate of the structural properties.

Analyses were performed using the pcGINA software for CMCs [49] to estimate the elastic composite properties of the vane material. The preform architecture used was a Y-shaped fabric manufactured by Techni-Weave and consolidated by BF Goodrich as reported in the work by Calomino et al. [10] and Brewer et al. [42]. Two types of weaves were used in the manufacturing of the vane blanks: five-harness satin weave (5H-SW) and plain weave (PW). Each of the 2D weaves had fibers running in orthogonal directions with a total fiber volume fraction of 40%. The CMC was coated on the outside by an Environment Barrier Coating (EBC) material. The locations of the CMC with the two weave patterns and that of the isotropic EBC material are shown in Figure 5. The estimated material properties of the vane material including the CLIP damage constants are listed in Table 1. In the absence of stress-strain data for the vane material the damage constants and nonlinear deformation used is the same as that of the 0101 CMC [28]. The stress-strain curve predicted for the 5H-SW and PW CMC used in the vane is compared with data from the 0101 CMC and shown in Figure 6.

Table 1 Material Properties of Vane CMC Constituents.

SiC/SiC (23°C)		5H-SW	PW	Coating
	E_l (GPa)	333	333	207
Fiber:	E_t (GPa)	173	173	
(Sylramic-iBN)	ν	0.20	0.17	0.20

	α (µm/m/°C)	2.7	2.7	2.77
	ε_f	0.0037	0.004	
	E_l (GPa)	300	200	
Matrix:	E_t (GPa)	300	200	
CVI/MI SiC	ν	0.20	0.125	
	α (µm/m/°C)	2.5	4.7	
	σ_0 (MPa)	226	226	
Damage	η_n	0.53	0.53	
constants	ρ_{nc}	-0.276	-0.276	
	ρ_{nn}	2.5	2.5	
Vol. frac. - fiber & coating (%)		40	40	
Vol. frac. - porosity (%)		5	5	
Stress free temp. (°C)		1450	1450	

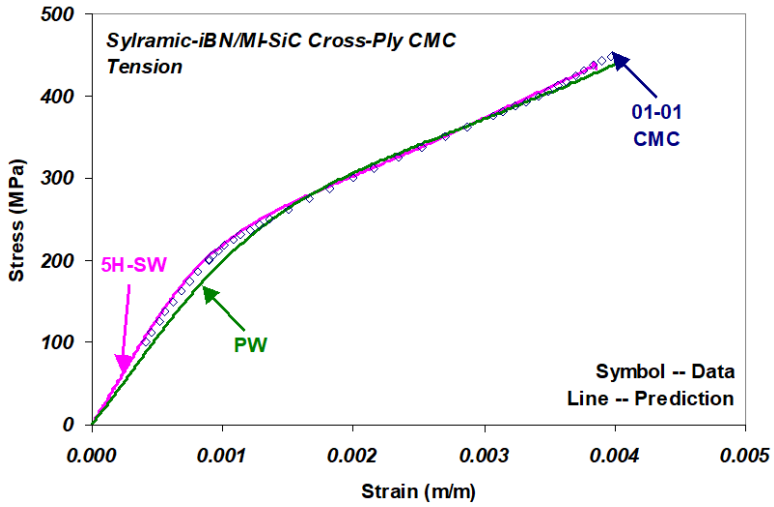

Figure 6 Predicted Stress-Strain Response of Vane CMC.

5. Analysis and Prediction of Pressurized Vane Tests

Figure 7 shows the 2D finite element mesh used in the analysis and the strain-gage locations corresponding to the test. The mesh consisted of 2917 nodes and 883 eight-node isoparametric plane-strain elements. Note that material properties of the composite vary throughout the vane (Figure 5). Fibers are oriented along the tangential (hoop) and the axial (out-of-plane) directions in the model. Thus, the 2D plane of the FE model consists of the hoop and radial (thru-thickness) material directions. At the trailing edge of the vane the hoop-direction fibers from the upper and lower arms of the vane meet in a 'Y' and round the central part of the trailing edge. The inner and outer regions of the trailing edge are packed with extra matrix material to give the vane the desired form. Matrix damage in the hoop and out-of-plane (axial) directions is considered in the analysis while the stress in the radial direction in the vane is used to estimate ply debond. Thus, even though the FE mesh is two-dimensional this damage analysis itself is three-dimensional.

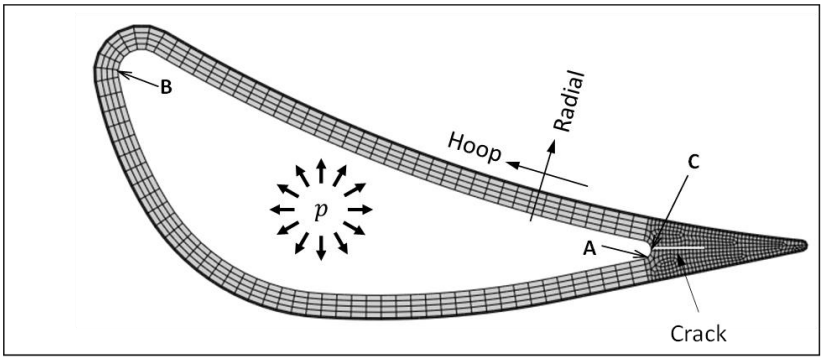

Figure 7 FEA Model of vane specimen showing delamination crack at inside of trailing edge.

FE analysis of the vane without a crack was done with uniform pressure load (p) applied along the entire inner surface in the model. Ply delamination was not considered. Results from the analysis for p = 2.0 MPa are shown in Figure 8. The hoop (S11) and axial (S33) stresses, shown in Figures 8(a) and 8(d), respectively, are high at the inside radii on both the leading and trailing edges (locations marked A and B in Figure 7), while the interlaminar stress (S22), shown in Figure 8(b) is highest at the inside radius of the trailing edge (location C in Figure 7). Figures 9(a) and 9(b) show variation of the damage functions η and ρ in the vane, respectively. It can be seen from the figures that matrix microcracking damage is significant at locations A and B, where the composite in-plane stresses are high. The maximum values of the in-plane stresses occur on the inside corner at the trailing edge near where the Y-cloth bifurcates. This is also the location where the matrix damage is most intense. Load is transferred to the fiber from the matrix as the latter cracks and eventually the fibers start to fail leading to the local failure of the composite. Consequently, the inside corner at the trailing edge near where the Y-cloth bifurcates will also be the region where the vane is expected to rupture when in-plane failure is the dominant failure mode.

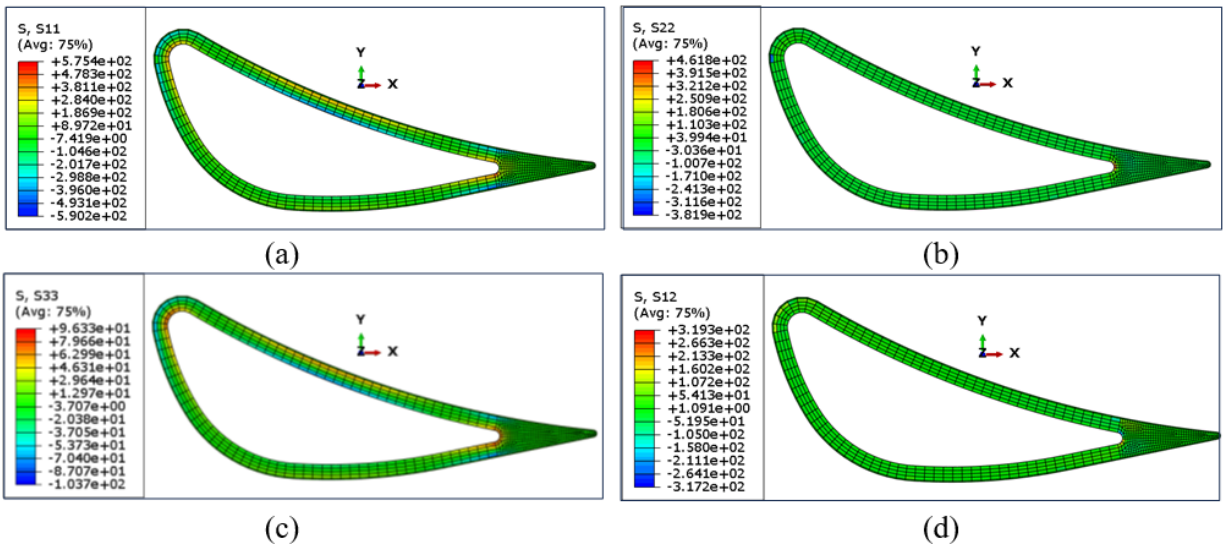

Figure 8 Predicted stress (MPa) state in CMC vane without crack for p = 2.0 MPa: (a) hoop stress, (b) axial stress, (c) radial stress, and (d) shear stress.

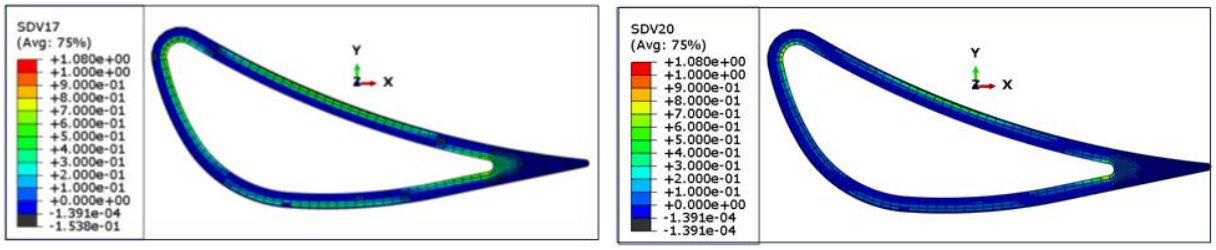

Figure 9 Predicted matrix damage in CMC vane without crack for p = 2.0 MPa: (a) η-function and (b) ρ-function.

Variation of the hoop stress at locations A and B, and at the location of strain gage-2 in the vane as the internal pressure is increased from zero to 2.0 MPa is shown in Figures 10. The corresponding growth in matrix damage at these locations in the vane is shown in Figure 11. The results show that microcracking damage in the matrix grows as the internal pressure is increased and that the material's load-strain response exhibits nonlinear behavior that corresponds to the growth in matrix damage.

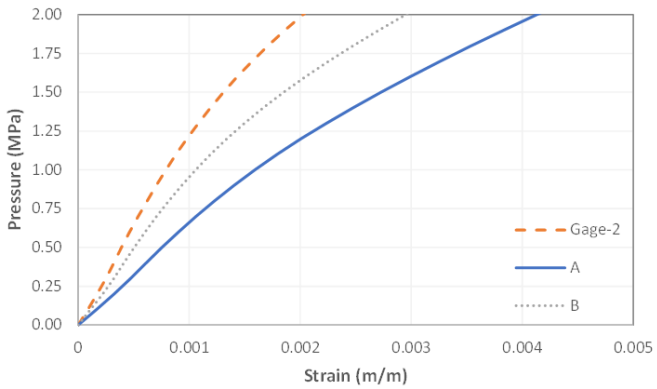

Figure 10 Predicted load-deformation behavior at strain gage-2, and locations A and B in the CMC vane.

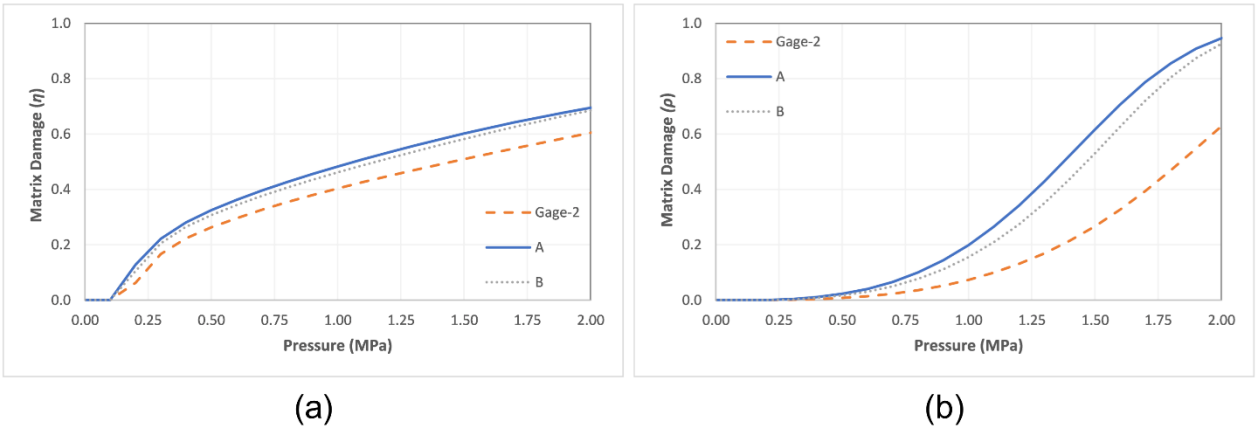

Figure 11 Predicted matrix damage at strain gage-2, and locations A and B in the CMC vane: (a) η-function and (b) ρ-function.

Figure 12(a) shows the measured and predicted strains in a test at five locations in one of the vane specimens as reported in Reference [42]. It is evident that, during the test, severe damage occurred at approximately 0.6 MPa applied pressure, resulting in abrupt change in strain-gage readings. The measured and predicted strains at two locations in a second vane specimen tested is shown in Figure 12(b). In this case sudden deviation from linear response occurs at about 0.3 MPa. As stated above, the effect of microdamage is included in the analysis results in Figures 12(a) and 12(b), but the model did not include representation of macrodamage such as delamination and gross matrix cracking.

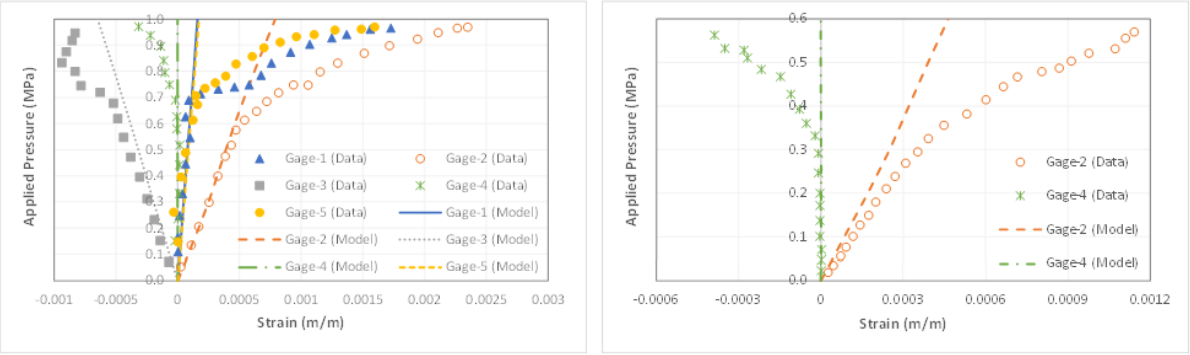

Figure 12 Predicted (without crack) and measured strains in (a) specimen-1 and (b) specimen-2.

Observation of the final condition of the burst test specimens (Figure 13) shows that final failure occurs by complete separation of the CMC material at the trailing edge. This is consistent with initiation and growth of an interlaminar crack at the trailing edge. Stress analysis indicates that the maximum value of the ILT occurs on the inside of the trailing edge (location C in Figure 7). This result suggests the formation of a crack on the inside of the trailing edge that grows across the trailing edge as the macromechanical damage mechanism responsible for the sudden change in strains shown in Figures 12(a) and 12(b). For pressure load of 0.6 MPa the through-thickness or ILT stress at the Y-cloth bifurcation location exceeds 30 MPa. This value seems sufficient to initiate a crack in a direction bisecting the trailing edge in the specimen whose results are shown in Figure 12(a).

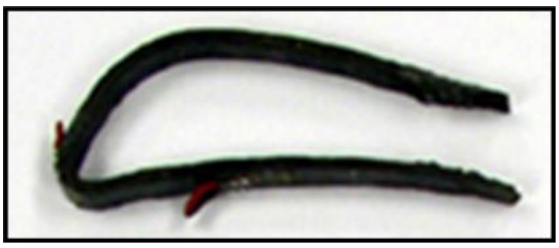

Figure 13 Typical final State of the Failed CMC Vane Specimens [31].

Thus, we attributed the nonlinearity in the strain-pressure curve seen after 0.6-MPa to be due to the initiation and subsequent growth of a crack at the Y-cloth bifurcation location (see Figure 7). By assuming that this was the only dominant crack in the vane we next used the strain data from gage-2 to determine the variation of crack length with the applied pressure. This plot, shown in Figure 14, was generated by solving a series of problems by the FE method, each with a different crack length,

such that the compliance of the vane is matched at gage-2 at each value of applied pressure. The broken lines in the figure represent compliance values corresponding to each crack length. It was further assumed that the final point on the gage-2 strain verses pressure plot corresponds to a crack length of 10-mm. This dimension was selected because it is the total length of the vane ahead of the bifurcation location of the Y-cloth. Note that Figure 14 is not a prediction, because data from the vane test was used to back out crack length versus load. To do a prediction, we would need the (fracture) resistance curve of the material obtained from a delamination test. Such data was not available.

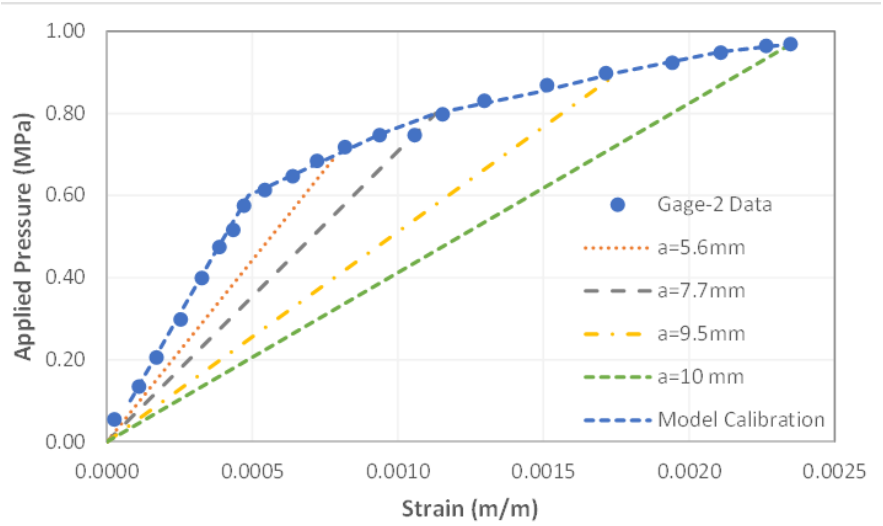

Figure 14 Calibration of strains at gage-2 using crack length.

In Figure 15, while gage-2 strains were used for calibration (because material toughness data was unavailable), the strains at the other strain-gage locations were predicted by the model using the above calibration, and seem to show general agreement with test data. Thus, the data from the strain-gages is consistent with the assumption of a dominant crack initiating at the inside of the trailing edge and growing across the section of the vane.

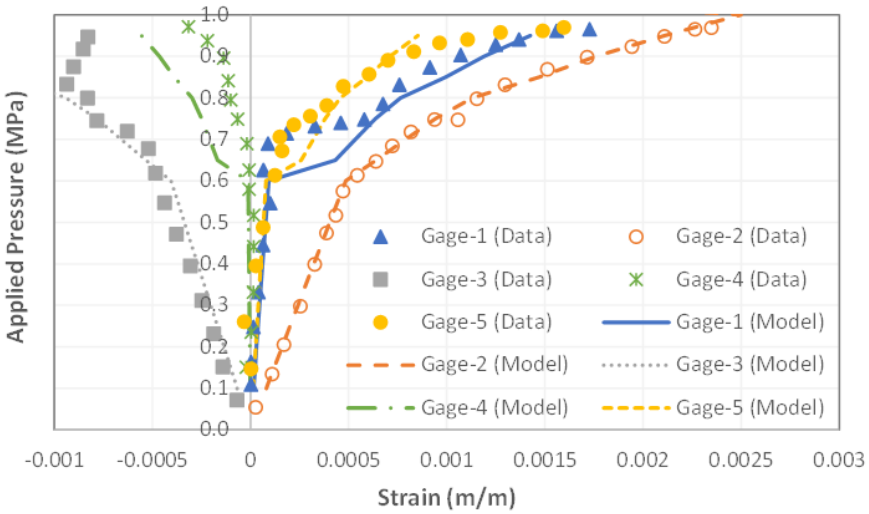

Figure 15 Predicted and measured strains at all strain-gages (with crack).

During each of the FE computations, with different crack lengths, the crack tip energy release rate (G) was also computed (using the path-independent J-integral method) for each crack length. Figure 16 shows the corresponding stress intensity factors (K) of the delamination crack that was determined from G. Extrapolation of the plot to a very small crack length gives a value around 5 MPa√m for K. Assuming that a small crack formed at an applied pressure approaching 0.6 MPa, the K at the tip of that crack would be around 5 MPa√m. Further increase in pressure would have caused that crack to initiate and grow in a stable fashion. The crack might have become unstable at some point after certain amount of crack growth. The initiation toughness value of 5 MPa√m is in close agreement with delamination toughness of 6 MPa√m inferred from C-channel tests done on the 0101 CMC material [50]. These values of fracture toughness are also similar to that of pure SiC at room temperature, which is reported to be 4.6 MPa√m in Reference [51].

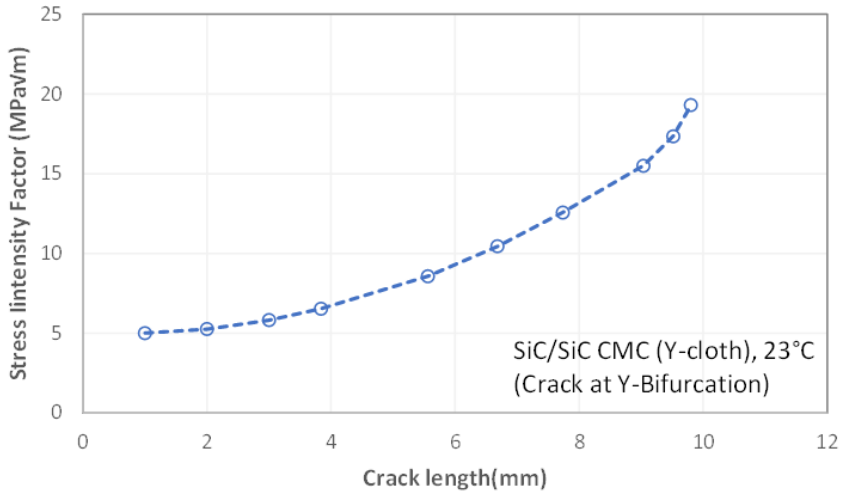

Figure 16 Computed stress intensity factors in CMC vane.

Note that the above fracture analyses assumed only a single crack. It is however possible that a second crack might have formed at some other location at some point during the pressure increase beyond 0.6 MPa.

6. Prediction of Time-Dependent Response and Life of CMC Vane

There were no test data available for the response of the vane under constant applied load at elevated temperature. The purpose of this analysis was therefore purely heuristic and simply intended to show how the CMC model described in this work could be used to life the CMC vane. In the analysis, the vane was loaded to an internal pressure of 0.5 MPa and held constant at a temperature of 1204°C. The load level selected is lower than the load at crack initiation for the vane specimen in Figure 12(a).

The material of the vane was taken to be the SiC/SiC composite of Table 1. Based on earlier modeling work [44], the time-dependent deformation mechanism was assumed to be creep of the matrix material. Stress analysis under constant load therefore requires knowledge of the creep law for the matrix. Typically, this can be deduced from strain data from at least two creep tests (at two stress levels) at the temperature of interest. Since this data was not available for the CMC material of the vane, we assumed the behavior of this material in creep to be identical to the 0101 CMC. The

time-dependent response of the SiC matrix at 1204°C in the 0101 CMC has been modeled previously [44] using the power-law creep law of equation (4) with $A = 1.427 \times 10^{-29}$ MPa^{-m} s^{-1}, $m = 7.1737$, $n = -1.8316$ and $\beta = 2.366 \times 10^{-11}$ s^{-1}, and shown to capture the time-dependent behavior of the composite over the stress range 110 MPa to 248 MPa. Similarly, oxidation constants for SiC fiber and SiC matrix reported in Reference [47] were used to model the effect of oxidation at 1204°C.

The finite element mesh shown in Figure 7 was used in the analysis. As described earlier the material properties of the composite vary throughout the vane (Figure 5). Matrix damage in the hoop (tangential) and the axial (out-of-plane) directions is considered during the load-up phase of the analysis. When the pressure load is held after it reaches the maximum value (0.5 MPa) creep deformation of the SiC matrix is considered. As it creeps it will shed load to the surrounding fibers and matrix resulting in stress redistribution throughout the structure.

Figure 17 shows the predicted time-dependent strain at two locations in the CMC vane: at gage-2, and at location A (Figure 7) in the vane where the hoop stress is the highest. There is rapid growth of creep strain initially. The growth strain of the strain soon becomes more gradual and approaches a constant value. The time variation of the hoop direction stress in the fiber at the same two locations is shown in Figure 18. The stress in the fiber is seen to increase continuously, both, due to matrix creep in which load is transferred to the fiber from the matrix, and by fiber oxidation in which stress increases as the cross section of the load-carrying part of the fiber gradually decreases.

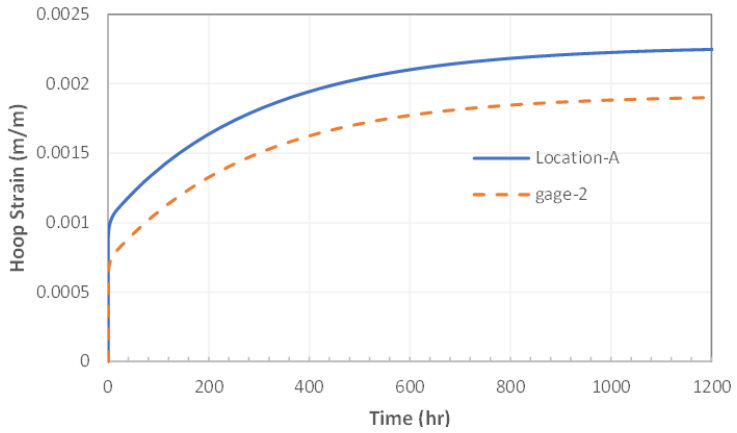

Figure 17 Predicted Change in hoop strain in CMC vane during creep.

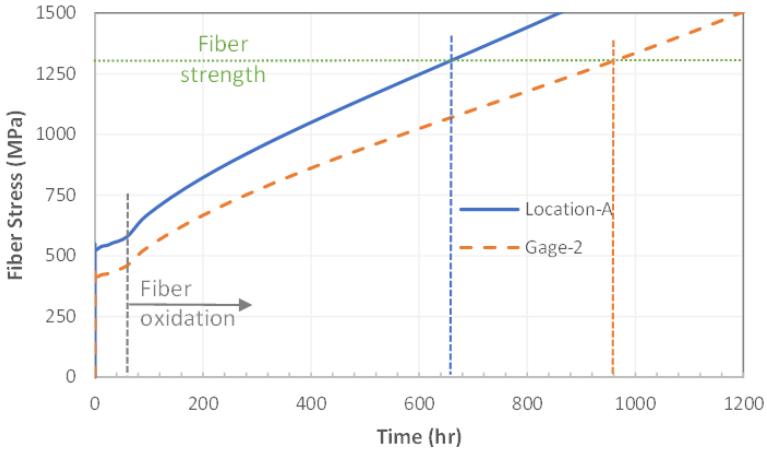

Figure 18 Fiber Stress and Life Prediction of the CMC vane under constant load.

The strength of the in-situ Sylramic™ SiC fiber in the 0101 CMC at 1204°C as determined in Reference [47] is also shown in Figure 18. The results are shown up to 1200 hours, which was how long the creep analysis, was run. Rupture of the CMC will be expected to occur when the fiber stress becomes equal to the fiber strength. From the figure we see that in this case the life would be about 660 hours (obtained by extrapolating the fiber hoop stress curve at Location-A to intersect the fiber failure plot). Similarly, according to the results shown in Figure 18, failure of the CMC at the location of strain gage-2 is expected to occur after 960 hours. Of course, local rupture of the CMC at location-A would result in redistribution the stresses in the vane and any subsequent failure.

Rupture life of the vane was also determined for various other values of applied internal pressure in the range between 0.3 and 0.6 MPa. The results from this study are shown in Figure 19, which shows that, as expected, higher loads correspond to lower rupture life. In fact, for the model predicts no failure even after 10,000 hours for internal pressure values lower than 0.32 MPa. As noted earlier, the experimental data showed that the vane fails by delamination at the bifurcation location of the Y-cloth for internal pressure values higher than 0.6 MPa.

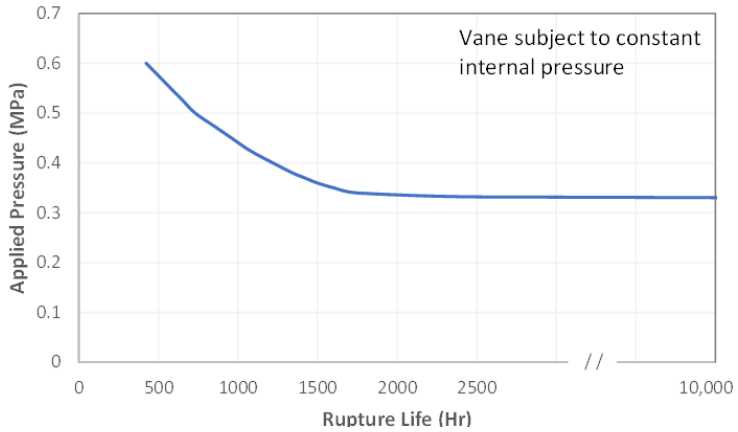

Figure 19 Effect of magnitude of internal pressure on rupture life of CMC vane under constant loading.

The effect of cyclic loading on the CMC vane was also investigated. Prior work [52] has shown that the deformation under fatigue loading depends only on the stress level and on the time the material is maintained at the stress level: the higher the stress and greater the time during which the material is exposed to stress, the larger the deformation. Besides the time at stress there is no other frequency effect on the deformation seen in this class of SiC/SiC CMC. It was also shown that the damage and creep model described earlier can predict deformation under cyclic loading.

However, cyclic loading does result in premature failure of the CMC as compared to constant loading either due to fatigue-induced damage of the coating material, due to interface abrasion that facilitates increased oxidation of fibers [53], or due to fatigue damage of the fibers [54]. Fatigue failure data from 0101 CMC was used in Reference [52] to obtain the following relationship between cycles to failure (N_f) and in-situ Sylramic™ SiC fiber strength (σ_{f0}):

$$\sigma_{f0}(\text{MPa}) = -10.94 \ln(N_f) + 793.49 \quad (5)$$

Since Equation (5) for the fiber was obtained by analyzing composite data, the effect of all three phenomena listed above that induces failure under fatigue is included in it.

Tension-tension fatigue study was done on the CMC vane using Equation (5) along with Equation (3c) to determine failure of the load-carrying fibers and, therefore, final failure of the CMC. Two values of load cycle frequency were considered: 1 Hz and 30 Hz. The ratio of minimum to maximum load (R-ratio) used in the study was 0.05. Change in maximum load on the fiber during each load cycle at location A in the vane with number of cycles for the 1 Hz and 30 Hz cases as determined by the model and corresponding to maximum internal pressure (p_{max}) equal to 0.5 MPa are shown in Figures 20(a) and 20(b), respectively. Also shown in these figures is the change in in-situ fiber strength according to Equation (5). Failure of the vane is predicted to occur after 400,000 cycles under 1 Hz fatigue loading, while at 30 Hz the vane is predicted to accumulate 10,000,000 cycles before failure. But as expected, failure of the vane subjected to 30 Hz fatigue loading occurs earlier (93 hours) than if the load is cycled at 1 Hz frequency (113 hours).

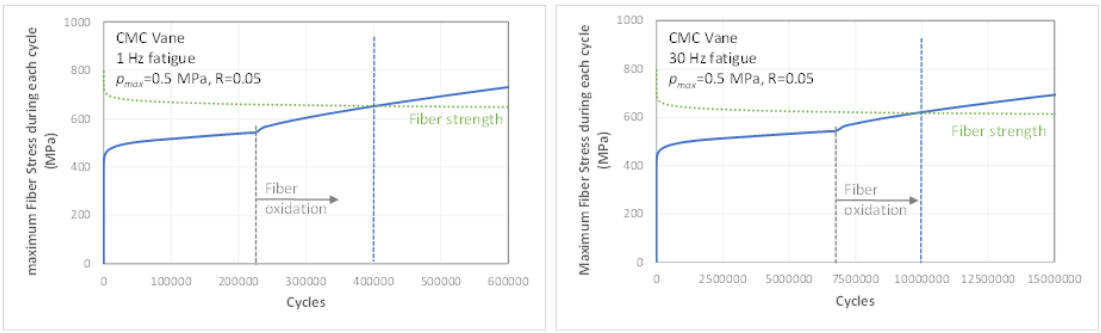

Figure 20 Fiber Stress and Life Prediction of the CMC vane under (a) 1 Hz and (b) 30 Hz cyclic load.

Figure 21 shows the predicted effect of the maximum value of cyclic internal pressure on fatigue life of the vane for the 1 Hz and 30 Hz frequency cases, each with R-ratio = 0.05. Smaller loads result in longer life. The load versus life behavior is seen to change abruptly for values of peak internal pressure less than 0.25 MPa and results in relative long rupture life. It is also seen that at each load level, the load cycled at 30 Hz frequency accumulates more cycles before failure as compared to 1 Hz frequency load cycling. Failure of the vane under cyclic loading is predicted to occur at location A in the vane just as in the constant load case.

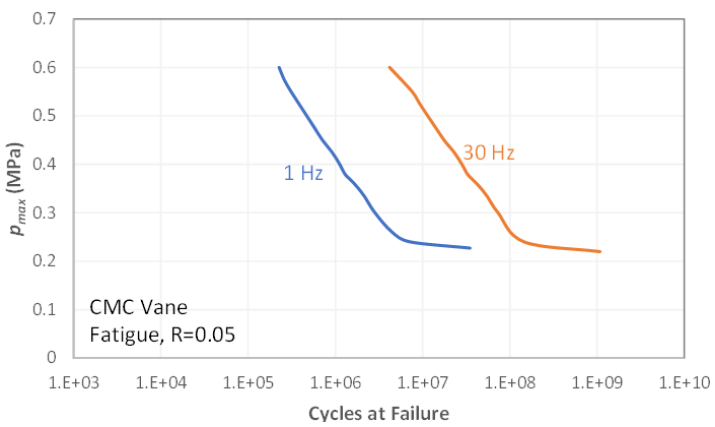

Figure 21 Effect of magnitude of internal pressure on rupture life of CMC vane under cyclic loading.

From the above results it can be noted that as the matrix creeps the local stress will decrease. Failure will occur when the local fiber stress reaches the strength of the fiber. Thus, in this example where the initial peak load is chosen to be smaller than that at crack initiation failure will likely occur due to failure of the hoop direction fibers. And unlike the burst test case, where failure occurred at the Y-cloth bifurcation location, in the time-dependent example failure is expected to occur near the inner radius location at the trailing and leading edges. This example thus shows that the nature of the applied load can change the mode of final failure of the CMC structure by affecting the amount of matrix microcracking and/or delamination.

7. Conclusion

A mechanistic modeling approach to analyzing 2D woven CMCs that considers the simultaneous effects of matrix microcracking, fiber fracture, time-dependent deformation of the constituents, and oxidation of the constituents has been used to model the burst test of CMC vanes. All the analysis and predictions of the vane were done using data from simple flat coupons. The model predicts that when in-plane damage is the dominant failure mode, the vane exhibits non-linear deformation behavior due to microcracking of the matrix. Analytical deformation results from the model are compared to test data obtained from experiments done on the vane at room temperature. Results of FE analysis using the CMC material model have been found to be consistent with the initiation and growth of a dominant delamination crack at the trailing edge leading to final failure. This assumption also explains the significant load carrying capacity of the CMC vane found to exist beyond crack initiation. The ability of the model to determine time-dependent deformation, damage and service life under constant loading and cyclic loading has been demonstrated. It is shown that constant loading is less deleterious to the life of the vane than fatigue loading. The higher the frequency of load cycles, the vane accumulates more cycles before failure, but the corresponding time to failure is shorter.

Acknowledgments

The authors would also like to thank Prof. Yasser Gowayed of the Department of Polymer and Fiber Engineering, Auburn University for determining the elastic constants of the CMC vane material using pcGINA.

Author Contributions

Both authors jointly conducted all the research work for this study.

Competing Interests

The authors have declared that no competing interests exist.

References

1. Karadimas G, Salonitis K. Ceramic matrix composites for aero engine applications-a review. Appl Sci. 2023; 13: 3017.

2. Boyle RJ, Parikh AH, Nagpal VK. Design considerations for ceramic matrix composite high pressure turbine blades. Proceedings of the ASME Turbo Expo 2019: Turbomachinery technical conference and exposition, volume 6: Ceramics; controls, diagnostics, and instrumentation; education; manufacturing materials and metallurgy; 2019 June 17-21; Phoenix, AZ, US. New York, NY, US: ASME. V006T02A014. doi: 10.1115/GT2019-91787.
3. Nakamura T, Oka T, Imanari K, Shinohara KI, Ishizaki M. Development of CMC turbine parts for aero engines. IHI Eng Rev. 2014; 47: 29-32.
4. Budiansky B, Hutchinson JW, Evans AG. Matrix fracture in fiber-reinforced ceramics. J Mech Phys Solids. 1986; 34: 167-189.
5. Gowayed Y, Ojard G. Ceramic matrix composites: Characterization, analysis, and applications. Lancaster, PA, US: Destech Publications Inc; 2020.
6. Brewer D. HSR/EPM combustor materials development program. Mater Sci Eng A. 1999; 261: 284-291.
7. Chen M, Qiu H, Xie W, Zhang B, Liu S, Luo W, et al. Research progress of continuous fiber reinforced ceramic matrix composite in hot section components of aero engine. IOP Conf Ser Mater Sci Eng. 2019; 678: 012043.
8. Halbig M, Jaskowiak M, Kiser J, Zhu D. Evaluation of ceramic matrix composite technology for aircraft turbine engine applications. Proceedings of the 51st AIAA aerospace sciences meeting including the new horizons forum and aerospace exposition; 2013 January 07-10; Grapevine (Dallas/Ft. Worth Region), TX, US. Reston, VA, US: American Institute of Aeronautics and Astronautics (AIAA).
9. Zawada L, Ojard G, Bouillon E, Spriet P, Logan C. Evaluation of ceramic matrix composite exhaust nozzle divergent seals. Proceedings of the 43rd AIAA/ASME/SAE/ASEE joint propulsion conference & exhibit; 2007 July 08-11; Cincinnati, OH, US. Reston, VA, US: American Institute of Aeronautics and Astronautics (AIAA).
10. Calomino A, Verrilli M. Ceramic matrix composite vane subelement fabrication. Proceedings of the ASME Turbo Expo 2004: Power for land, sea, and air, volume 2: Turbo Expo 2004; 2004 June 14-17; Vienna, Austria. New York, NY, US: ASME.
11. Vedula V, Shi J, Jarmon D, Ochs S, Oni L, Lawton T, et al. Ceramic matrix composite turbine vanes for gas turbine engines. Proceedings of the ASME Turbo Expo 2005: Power for land, sea, and air, volume 1: Turbo Expo 2005; 2005 June 06-09; Reno, NV, US. New York, NY, US: ASME.
12. Zawada L, Jones E, Jefferson G, Pierce JL, Witlow T. Damage progression in generic ceramic matrix composite turbine airfoils. US Air Force; 2022; AFRL-RX-WP-TR-2022-0037. Available from: https://apps.dtic.mil/sti/pdfs/AD1161002.pdf.
13. Liu X, Zhao W, Guo H, Su Y, Li L, Liu C. XCT damage evaluation and analysis of SiC/SiC turbine guide vanes after thermal shocks. Int J Appl Ceram Technol. 2023; 20: 2919-2919.
14. Spring SD, Hogan MT, Lewis DA, Steibel JD, Kinney S. 2006, Application of uncooled ceramic matrix composite power turbine blades for performance improvement of advanced turboshaft engines. Proceedings of the American helicopter society 62nd annual forum; 2006 May 9-11; Phoenix, AZ, US. Fairfax, VA, US: American Helicopter Society.
15. Guo X, Xu Y, Li J, Luo X, Li L, Hu X. Damage monitoring of SiC/SiC turbine blisk under overspeed rotation testing using X-ray computed tomography and natural frequency. Proc Inst Mech Eng L. 2023. doi: 10.1177/14644207231205875.

16. Luthra KL, Corman GS. Melt infiltrated (MI) SiC/SiC composites for gas turbine applications. In: High temperature ceramic matrix composites. Hoboken, NJ, US: John Wiley & Sons; 2001. pp. 744-753. doi: 10.1002/3527605622.ch113.
17. Chamberlain A, Lane J. SiC/SiC ceramic matric composites: A turbine engine perspective. Proceedings of the ultra-high temperature ceramics: Materials for extreme environmental applications II; 2012 May 13-18; Hernstein, Austria. New York, NY, US: Engineering Conferences International (ECI). Available from: http://dc.engconfintl.org/uhtc/7.
18. Rolls-Royce. Rolls-Royce reaches new milestone as world's largest aero-engine build starts [Internet]. Manchester, UK: Rolls-Royce; 2021. Available from: https://www.rolls-royce.com/media/press-releases/2021/29-03-2021-rr-reaches-new-milestone-as-worlds-largest-aero-engine-build-starts.aspx.
19. Gardiner G. Pratt & Whitney to produce advanced metal and CMC turbine airfoils in North Carolina [Internet]. Cincinnati, OH: Composites World; 2021. Available from: https://www.compositesworld.com/articles/pratt-whitney-to-produce-advanced-metal-and-cmc-turbine-airfoils-in-north-carolina.
20. Steibel J. Ceramic matrix composites taking flight at GE aviation. Am Ceram Soc Bull. 2019; 98: 30-33.
21. Grandt AF. Fundamentals of structural integrity: Damage tolerant design and nondestructive evaluation. Hoboken, NJ, US: John Wiley & Sons; 2004.
22. Jefferson G, Przybyla C, Zawada l. Preface: Assessment of damage progression models for SiC/SiC ceramic matrix composites. Int J Multiscale Comput Eng. 2021; 19: v-xiv. doi: 10.1615/IntJMultCompEng.2021041807.
23. Genin GM, Hutchinson JW. Composite laminates in plane stress: Constitutive modeling and stress redistribution due to matrix cracking. J Am Ceram Soc. 1997; 80: 1245-1255.
24. Camus G. Modelling of the mechanical behavior and damage processes of fibrous ceramic matrix composites: Application to a 2-D SiC/SiC. Int J Solids Struct. 2000; 37: 919-942.
25. Pailler F, Lamon J. Micromechanics based model of fatigue/oxidation for ceramic matrix composites. Compos Sci Technol. 2005; 65: 369-374.
26. Baxevanis T, Charalambakis N. A micromechanically based model for damage-enhanced creep-rupture in continuous fiber-reinforced ceramic matrix composites. Mech Mater. 2010; 42: 570-580.
27. Yang CP, Jiao GQ, Wang B. Modeling oxidation damage of continuous fiber reinforced ceramic matrix composites. Acta Mech Sin. 2011; 27: 382-388.
28. Santhosh U, Ahmad J. A model for estimating nonlinear deformation and damage in ceramic matrix composites. J Compos Mater. 2013; 47: 1257-1272.
29. Liu H, Yuan H, Yang Z. Damage modeling of oxide/oxide ceramic matrix composites under cyclic loading conditions. Ceram Int. 2020; 46: 23379-23389.
30. Mital SK, Arnold SM, Bednarcyk BA, Pineda EJ. Micromechanics-based modeling of SiC/SiC ceramic matrix composites and structures. Recent Prog Mater. 2023; 5: 025.
31. Chaboche JL, Maire JF. A new micromechanics based CDM model and its application to CMC's. Aerosp Sci Technol. 2002; 6: 131-145.
32. Maire JF, Lesne PM. A damage model for ceramic matrix composites. Aerosp Sci Technol. 1997; 1: 259-266.

33. Ladevèze P. A damage computational method for composite structures. Comput Struct. 1992; 44: 79-87.
34. Ladevèze P, Gasser A, Allix O. Damage mechanisms modeling for ceramic composites. J Eng Mater Technol. 1994; 116: 331-336.
35. Shojaei A, Li G, Fish J, Tan PJ. Multi-scale constitutive modeling of ceramic matrix composites by continuum damage mechanics. Int J Solids Struct. 2014; 51: 4068-4081.
36. Shah SZ, Megat Yusoff PS, Karuppanan S, Choudhry RS, Sajid Z. Multiscale damage modelling of 3D woven composites under static and impact loads. Compos Part A Appl Sci Manuf. 2021; 151: 106659.
37. Artz T, Yuan Z, Kumar R, Fish J. Computational model for oxidation-assisted rupture of ceramic matrix composites. Int J Solids Struct. 2020; 202: 195-207.
38. Letombe S, Cluzel C, Ladevèze P. A macroscopic model coupling oxidation and damage for CMCs. Proceedings of the JNC13 conference; 2003 March 12-14; Strasbourg, France. Manassas, VA, US: Institute of Navigation.
39. Sadowski T, Marsavina L. Multiscale modelling of two-phase ceramic matrix composites. Comput Mater Sci. 2011; 50: 1336-1346.
40. Borkowski L, Kumar RS. Assessment of a micromechanics-based progressive damage and creep model applied to ceramic matrix composites with holes. Int J Multiscale Comput Eng. 2021; 19: 35-59.
41. Bednarcyk BA, Arnold SM. MAC/GMC 4.0 user's manual-keywords manual. Washington DC, US: NASA; 2002; NASA/TM 2002-212077.
42. Brewer DN, Verrilli M, Calomino A. Ceramic matrix composite vane subelement burst testing. Proceedings of the ASME Turbo Expo 2006: Power for land, sea, and air, volume 2: Aircraft engine; ceramics; coal, biomass and alternative fuels; controls, diagnostics and instrumentation; environmental and regulatory affairs; 2006 May 8-11; Barcelona, Spain. New York, NY, US: ASME.
43. Karandikar P, Chou TW. Characterization and modeling of microcracking and elastic moduli changes in Nicalon/CAS composites. Compos Sci Technol. 1993; 46: 253-263.
44. Santhosh U, Ahmad J, Kalarikkal S, Ojard G, Gowayed Y. Time-dependent deformation and damage modeling of a SiC/SiC composite. J Aerosp Eng. 2018; 31: 04018086. doi: 10.1061/(ASCE)AS.1943-5525.0000921.
45. Santhosh U, Ahmad J, Ojard G, Miller R, Gowayed Y. Deformation and damage modeling of ceramic matrix composites under multiaxial stresses. Compos B Eng. 2016; 90: 97-106.
46. Al Nasiri N, Patra N, Ni N, Jayaseelan DD, Lee WE. Oxidation behaviour of SiC/SiC ceramic matrix composites in air. J Eur Ceram Soc. 2016; 36: 3293-3302.
47. Santhosh U, Ahmad J, Ojard G, Gowayed Y. A synergistic model of stress and oxidation induced damage and failure in silicon carbide-based ceramic matrix composites. J Am Ceram Soc. 2021; 104: 4163-4182.
48. Santhosh U, Ahmad J, John R, Ojard G, Miller R, Gowayed Y. Modeling of stress concentration in ceramic matrix composites. Compos B Eng. 2013; 45: 1156-1163.
49. Gowayed Y, Yi L. Mechanical behavior of textile composite materials using a hybrid finite element approach. Polym Compos. 1997; 18: 313-319.

50. Miller RJ, Ojard GC, Ahmad J, Santhosh U, Gowayed YA. Durability and life prediction of ceramic matrix composites, volume 1. Model development and test validation. Final Technical Report. US Air Force; 2006; No. F33615-01-C-5234.
51. Munro RG, Freiman SW, Baker TL. Fracture toughness data for brittle materials. Gaithersburg, MD, US: US Department of Commerce, National Institute of Standards and Technology; 1998; NISTIR 6153.
52. Santhosh U, Ahmad J, Ojard G, Gowayed Y. Modeling deformation of a melt-infiltrated SiC/SiC composite under fatigue loading. Ceram Int. 2022; 48: 6574-6590.
53. Zhu S, Mizuno M, Kagawa Y, Mutoh Y. Monotonic tension, fatigue and creep behavior of SiC-fiber-reinforced SiC-matrix composites: A review. Compos Sci Technol. 1999; 59: 833-851.
54. Chawla N, Kerr M, Chawla KK. Monotonic and cyclic fatigue behavior of high-performance ceramic fibers. J Am Ceram Soc. 2005; 88: 101-108.